Carbon 152 (2019) 643–651

Contents lists available at ScienceDirect

Carbon

journal homepage: www.elsevier.com/locate/carbon

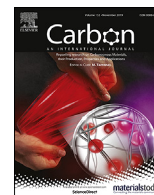

Femtosecond light pulse response of photodetectors based on Graphene/n-Si heterojunctions

M. Scagliotti [a, b], M. Salvato [a, b, *], M. De Crescenzi [a, b], N.G. Kovalchuk [c], I.V. Komissarov [c, d], S.L. Prischepa [c, d], D. Catone [e], L. Di Mario [e], M. Boscardin [f], M. Crivellari [f], P. Castrucci [a, b]

[a] *Dipartimento di Fisica, Università di Roma 'Tor Vergata', Via della Ricerca Scientifica 1, 00133 Roma, Italy*
[b] *INFN, Università di Roma 'Tor Vergata', Via della Ricerca Scientifica 1, 00133 Roma, Italy*
[c] *Belarusian State University of Informatics and Radioelectronics, P. Browka 6, Minsk 220013, Belarus*
[d] *National Research Nuclear University MEPhI, Kashirskoe highway 31, Moscow, 115409, Russia*
[e] *ISM-CNR, Division of Ultrafast Processes in Materials (FLASHit), Via del Fosso del Cavaliere 100, 00133 Roma, Italy*
[f] *Micro-nano Characterization and Fabrication Facility, Fondazione Bruno Kessler (FBK), Via Sommarive 18, 38123 Povo-Trento, Italy*

A R T I C L E I N F O

Article history:
Received 3 April 2019
Received in revised form
31 May 2019
Accepted 12 June 2019
Available online 12 June 2019

A B S T R A C T

To take advantage of the graphene appealing electronic properties, in this work we present a photodetector (PD) based on graphene/n-silicon heterojunction (GSH). In this device, graphene acts as light transmitter, counter electrode junction element and photocarrier collector. The photodetector has been provided with metal contacts allowing either photovoltaic or photoconductive operation mode. We investigated the response of GSH PD to a 35-femtosecond laser pulse. In the photovoltaic configuration, the PD exhibits rise times of some tens of nanoseconds, detecting light from ultraviolet (275 nm) to infrared (1150 nm). In photoconductive mode applying a gate voltage V_G, the external quantum efficiency hugely increases, from a value of 2% up to 200%. Together with the observation of a rise time, that decreases down to a minimum value of about 1 ns, this makes our device even more competitive and comparable with commercial photodetectors.

© 2019 Elsevier Ltd. All rights reserved.

1. Introduction

Thanks to its fascinating features [1] graphene is nowadays emerging as a real material for future nano optoelectronics [2]. The advantage of its use is to have an atomic-scale thickness material with unique properties: mechanical strength and flexibility, air stability, heat and electrical conductivity, optical transparency. In addition, thanks to the compatibility with Silicon and other conventional materials [3], the use of graphene has been theorized in electronic devices that involve the electric field effect, due to its high room-temperature charge mobilities of $10^5\ cm^2/V\cdot s$ [4]. Graphene has already been successfully used for the realization of opto-electronic devices like graphene/GaAs van der Waals heterostructure solar cells [5], graphene-silicon Schottky junction solar cells [6–8], as composite material together with carbon nanotubes for holes transporting layer in solar cells [9] and high responsivity photodetectors (PDs) [10]. Above all, the request for PDs is very high, because light detection is a fundamental issue in optical sensing, in particular infrared (IR) PDs are strongly required for a large class of medical [11], industrial, imaging, communication [12] and scientific purposes [13]. In addition, also the ultraviolet (UV) radiation has a great impact in many important aspects of daily life and scientific research: for example, in the stratospheric ozone monitoring, promoting the synthesis of vitamin D, killing germs [14], etc. Therefore, it is very meaningful to get a single optimized device able to detect wide-spectrum light from UV to IR with a fast response and high responsivity.

However, due to the atomic thickness of monolayer graphene, resulting in inefficient absolute light absorption (single sheet optical absorbance is about 2.3% at 550 nm [15]) and consequently high optical transparency, a PD based only on graphene would present a very low responsivity. To overcome this issue, different approaches have been proposed and realized: light-trapping techniques [16], integration of graphene into nanocavities [17], microcavities [18] or wave guide [19], hybrid graphene-quantum dot structures [20]. All these methods increase the photo-responsivity

* Corresponding author. Dipartimento di Fisica, Università di Roma 'Tor Vergata', Via della Ricerca Scientifica 1, 00133 Roma, Italy.
E-mail address: matteo.salvato@roma2.infn.it (M. Salvato).

https://doi.org/10.1016/j.carbon.2019.06.051
0008-6223/© 2019 Elsevier Ltd. All rights reserved.

of graphene but reduce the response speed or the detection active area and the electronic bands. Moreover, these graphene-based devices are often very expensive and difficult to obtain, especially for large-scale production, making them usable only in particular conditions. Another possible strategy is to combine it with a material with a high light absorption coefficient that is already industrially ready and well-studied to allow rapid development of this new technology. For these reasons, a heterostructure composed of graphene and Silicon can be a valid candidate for new PD technology [6–8]. Such hybrid devices combine the high visible light absorption of Silicon, and its ease of being industrially produced and managed, with the advantage of the high electronic charge mobility of graphene for fast response time. The response speed of Graphene/Si PDs has been improved in recent years up to rise time of the order of several ns [21]. In this work, we present a three-terminal PD device composed of a Graphene/n-Silicon heterojunction (GSH) (Fig. 1) which can work in Photovoltaic (PV) or Photoconductive (PC) mode. The reported measurements of the characteristics of a PD show that this device works effectively as a multicolour high responsivity PD that exhibits response times of the order of nanoseconds when it is lighted by femtosecond laser pulses.

2. Experimental

2.1. Samples preparation

Silicon substrates with metal electrodes have been provided by Fondazione Bruno Kessler [22] and successfully used for carbon nanotubes/Si solar cells [23] and PDs [24]. The PD realization scheme is based on a top-down design (Fig. 1a–c): the substrates are composed of a n-doped Silicon wafer with a thickness of 100 μm and an electrical resistivity of 0.53 Ω cm (donor concentration atoms $N_D \approx 10^{16}$ cm^{-3}). The bottom surface is covered with a Cr/Au metallic layer forming an Ohmic contact with the Si. On the top surface, two sets of Cr/Pt interdigitated electrodes, composed by 10 fingers distant $D = 250$ μm each other (width 50 μm each) alternately connected to the two separated electrodes S and D, are deposited on a 300 nm thick SiO_2 template layer and are electrically isolated by the Si substrate. The designed multifinger geometry of the interdigitated electrodes is used to reach the maximum collection of photogenerated charges [25]. In the last phase of the PD manufacturing process, a film composed by 2–3 layers of graphene was deposited on the top side of the substrate resulting in contact with the interdigitated electrodes and with the Si surface. The graphene forms then a heterojunction with silicon creating the active area ($A = 0.08$ cm^2) of the detector.

Graphene growth was performed through a chemical vapour deposition (CVD) process at atmospheric pressure on both sides of a copper foil using n-decane as precursor and a mixture of nitrogen and hydrogen as gas carriers [26]. After the growth, the graphene has been transferred onto the n-Si substrates by a wet-chemical two-stage process at room temperature. The first step consists in etching one side of the copper foil by oxygen plasma in order to remove “unwanted” graphene. Subsequently the copper foil has been completely dissolved in a solution of water and $FeCl_3$ [27]. The obtained graphene film has been kindly washed many times in a distilled water bath. Two parts of the same graphene sheet have been transferred on a glass and on the silicon substrate [26]. Prior to transfer graphene, an etching with hydrofluoric acid (HF) was performed to remove native oxide on the silicon surface. The final device has 3 external controls (see Fig. 1a–c) given by the *Gate* electrode (G), placed in contact with the silicon, and by the interdigitated *Source* (S) and *Drain* (D) electrodes in contact with Graphene. For this reason, there are two different operating configurations that can be exploited in photo detection: photovoltaic (PV, Fig. 1a), where the photogenerated charges crossing the junction are collected by the bottom and the top electrodes (G and the short circuited S and D), and photoconductive (PC, Fig. 1b), where the photocharges travelling across the graphene layer are collected by the S and D electrodes.

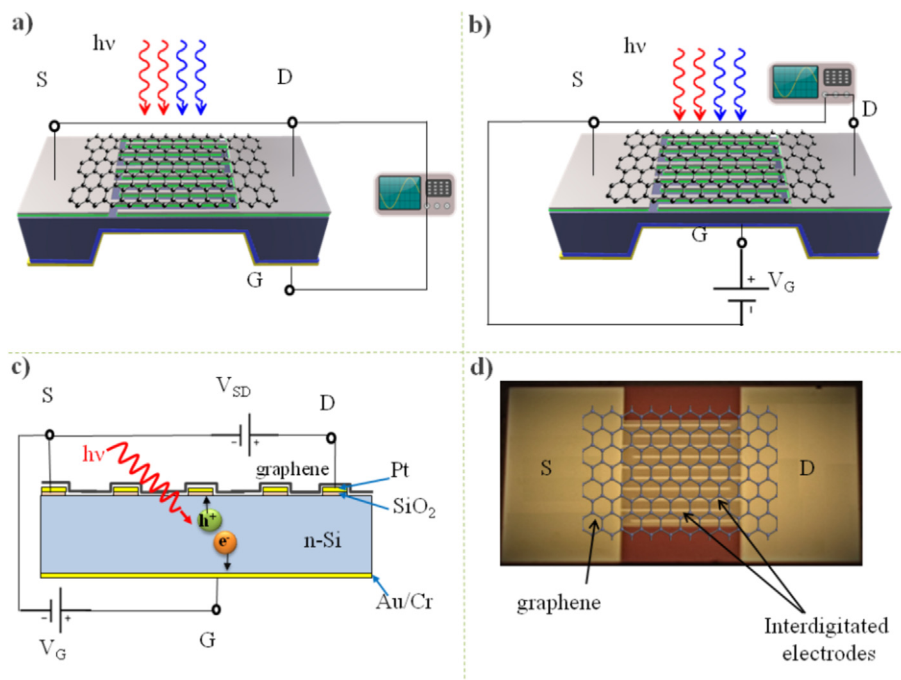

Fig. 1. **a)** 3D device schematic in photovoltaic (PV) and **b)** in photoconductive (PC) configuration; **c)** voltage doping mechanism under illumination in PC mode; **d)** optical top view of the device. The graphene layer, transparent at optical wavelengths, is substituted by its lattice sketch. (A colour version of this figure can be viewed online.)

An optical image of the top side of the sample is shown in Fig. 1d. The interdigitated electrodes connected to the S and D terminals are easily distinguished from the graphene deposited sheet which appears transparent under visible light and it is substituted by a lattice sketch in the figure.

2.2. Samples characterization

Raman spectra, not shown here, were acquired on graphene sheets before transferring on the Si substrates [26]. The measurements were performed using a 473 nm excitation laser and show that the grown graphene mainly is double layer with minor fractions of single layer and three layers. The optical transmittance of the graphene deposited on the glass substrate is 94% at a photon wavelength of 550 nm. This value corresponds to a number of graphene layers between 2 (95.5%) and 3 (93.3%) [26]. The slight discrepancy between the optical and Raman measurements can be explained as the result of possible formation of twisted structures as a consequence of the graphene transfer on the glass substrate [26].

After the transfer on the Si substrate, scanning tunnelling measurements (STM) were performed on the graphene surface in contact with Si. Fig. 2a shows a typical STM image of the sample where some graphene sheets can be observed. The blow-up of the image shows the graphene hexagonal structure as highlighted by the stick-and-ball sketch with a measured distance between the next neighbouring atoms of 0.14 nm. This value corresponds to a lattice parameter of 0.24 nm, which is in very good agreement with the lattice parameter of graphene [1]. Scanning tunnelling spectroscopy (STS) was performed during the STM analysis by acquiring current-voltage (*I-V*) characteristics and by mapping the density of the filled and empty electronic states (with respect to the Fermi level E_F) of the analyzed surface. A typical *I-V* measurement is reported, together with the differential conductance vs. voltage, in Fig. 2b. The finite value of the zero voltage conductance (corresponding to E_F) confirms a sizeable metallic character of the graphene deposited on the Si surface [1,3].

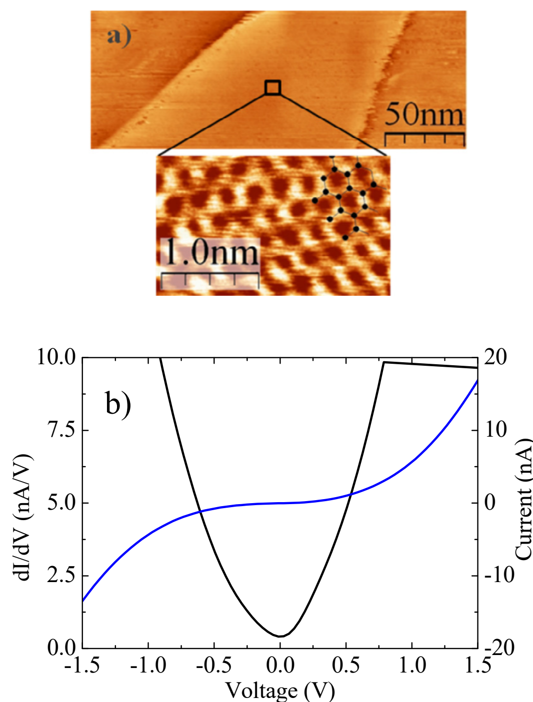

Fig. 2. a) STM imaging, acquired ad 0.5 nA and 0.5 V, of the graphene deposited on the n-Si and blow-up of a selected area with the stick-and-ball sketch for tracing the atomic structure; b) typical tunnelling current-voltage (blue line-right scale) and differential conductance-voltage (black line-left scale) characteristics of the selected graphene area. The zero voltage corresponds to the Fermi level separating the filled and empty electronic states of graphene. (A colour version of this figure can be viewed online.)

The PDs were characterized by d.c. *I-V* measurements in dark conditions using a Keithley 2602A source/meter and for the responsivity measurements a calibrated light emitter diode (LED Kingbright L-7113QBC-D, emission spectrum peaked at $\lambda = 460$ nm) has been used as light source. The photoresponse was also measured as a function of the wavelength of the incident light in the range $\lambda = 300$ nm−1000 nm using an Ametek 7265 lock-in amplifier for acquiring the signal from the sample and from the detector after being illuminated by a modulated light emitted by a LOT LSE 140 Xenon lamp and passing through a monochromator (LOT MSH-300).

To investigate the potential of our devices in fast signals detection, a femtosecond pulsed laser source was used. The laser system consists of a chirped pulse amplifier, seeded by a Ti:Sa oscillator and coupled with an Optical Parameter Amplifier [28] that produces 40 fs pulses in a wide energy range (from 240 nm to 20 μm with a repetition rate of 1 kHz) [29,30] and used as tunable ultra short light source. In this case, the signal is acquired by a 30 GHz Tektronix oscilloscope using coaxial cables connected to the sample terminals, without the use of any filter or amplifier, and terminated on the 50 Ω oscilloscope internal resistance.

3. Experimental results

3.1. Photovoltaic configuration

In PV mode (Fig. 1a) the detector works as a two-terminal device: an electric current between the electrode G and the two top electrodes S and D connected together, is measured. In this condition, when the device is not illuminated, the *J-V* feature (Fig. 3a, black line) proves the rectifying properties of the graphene/silicon heterojunction. This shows a dark current density of few mA/cm^2 slowly increasing with the reverse applied voltage. Illuminating the sample with 100 mW/cm^2 white light (Fig. 3a, red curve), a shift of the reverse polarized curve is observed due to the generation of the photocurrent indicating the possibility to use this device for photodetection applications.

In order to evaluate the PD's performance in PV mode, measurements were carried out in short-circuit condition ($V = 0$) lighting the device with a calibrated LED. Fig. 3b shows the short circuit current density J_{sc}, measured with respect to its value in dark conditions J_{sc0}, as a function of the incident light power density P_{opt}. The line is a fit to the data using a power law $x^{1.08}$ which indicates a very good linearity of the PD response. The gain between input and output has been estimated through the responsivity given by $R = (J_{sc} - J_{sc0})/P_{opt}$. The calculation gives $R \approx 0.7$A/W, which is of the same order of commercial photodetectors [31] and results weakly dependent on P_{opt}.

The response speed of the device has been investigated using the femtosecond pulsed laser as light source. In Fig. 4, a typical PD response to a single laser pulse (with incident wavelength $\lambda = 532$ nm and energy $E = 10$ nJ) is reported. The rise time (τ_r), defined as the time difference between the 90% and 10% of the full-scale signal, is shown in the inset for different wavelengths at $E = 10$ nJ. From this figure emerges the ability of the device to detect a fast multicolour signal, responding with times of the order of tens of nanoseconds. Interestingly, τ_r is almost constant for $\lambda \leq 450$ nm and increases for higher wavelengths suggesting two different mechanisms in light absorption as will be discussed below. Here we

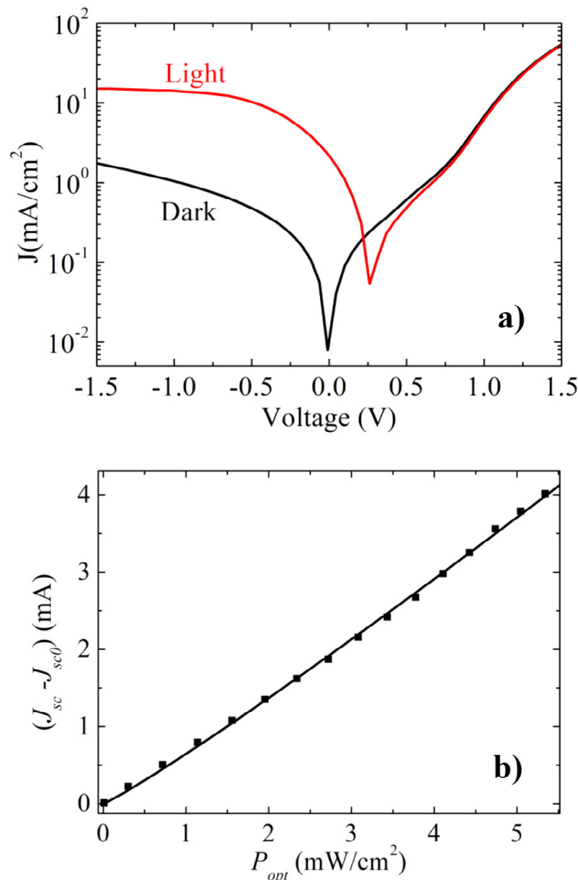

Fig. 3. a): *J*–*V* characteristic of the device acquired in dark conditions (PV mode); b): schort circuit photocurrent vs. incident optical power in PV mode. The line is a fit to the data using the power law x^y with $y = 1.08$. (A colour version of this figure can be viewed online.)

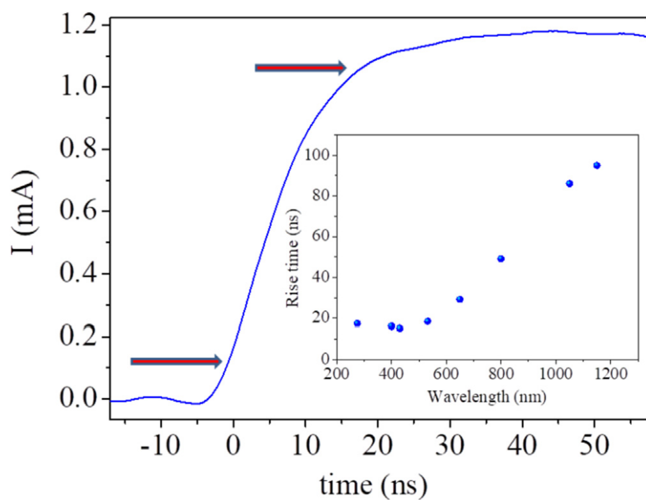

Fig. 4. Typical PD response in PV mode to a single 35 fs laser pulse. The arrows indicate the 10% and the 90% of the pulse height used as a criterion for the rise time estimation; inset: rise time vs. wavelength in PV mode under 35 fs pulsed laser source for incident light energy $E = 10$ nJ. (A colour version of this figure can be viewed online.)

emphasize that these results are obtained using the detector in PV mode without spending energy and without the use of any external electronic amplification. This is essential in applications where it is important to keep down not only the energy expenditure but also the size and weight of the detection system.

3.2. Photoconductive configuration

In PC mode the detector works as a three-terminal device. In this configuration, the output current signal is recorded between the top S and D electrodes, both connected with the graphene layer (Fig. 1b). The electrode G, which is on the bottom side of the detector, is instead used as an external input control through an electric gate potential. For $V_G > 0$ the GSH is reverse polarized and an injection of positive charges (holes) occurs inside the graphene (Fig. 1c). A further contribution to the current possibly comes from electrons in graphene that cross the Si/graphene barrier interface after the n doping of graphene layer due to the reverse voltage V_G applied across the junction [6].

The I_{SD} vs. V_G characteristics at different applied values of V_{SD} in dark conditions are shown in Fig. 5. The curves represent the typical trend of a 3-terminal device: at low V_G (up to about 4 V) the current weakly depends on V_G, but when a certain value of V_G is exceeded, an increase of the current flowing inside the graphene is observed. In this configuration, the minority charges (holes) of the n-Si region flow towards the graphene driven by the built-in potential V_{bi}, generated at graphene/n-Si interface, and by V_G. In addition to a leakage current, which contributes in a linear manner to the I_{SD} vs. V_G characteristics, an avalanche mechanism can be invoked for taking into account the nonlinear trend of the curves that becomes more pronounced as V_G increases above 4 V. It is important to note that the beginning of the avalanche region occurs at $V_G \approx 4$ V, which is a considerable low value especially if compared to commercial photodetectors that need even a 100 V bias to reach this operating point [31].

To examine the 3-terminal device behaviour, measurements of external quantum efficiency (EQE) have been performed in the wavelength range of the incident light between $\lambda = 300$ nm and $\lambda = 1000$ nm. The EQE is defined by the expression $EQE = (hcJ_{sc})/(q\lambda P_{opt})$ where h is the Planck constant, c is the speed of light and J_{sc} the short circuit current density. The results are shown in Fig. 6a. In the absence of a gate voltage the typical EQE shape of a p-n Si junction can be noticed [32], indeed in this case we

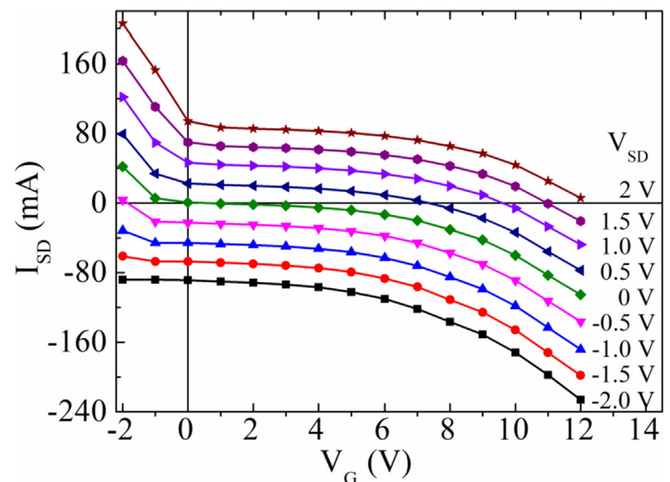

Fig. 5. Source-drain current I_{SD} vs. gate voltage V_G acquired in dark conditions for different values of V_{SD}. (A colour version of this figure can be viewed online.)

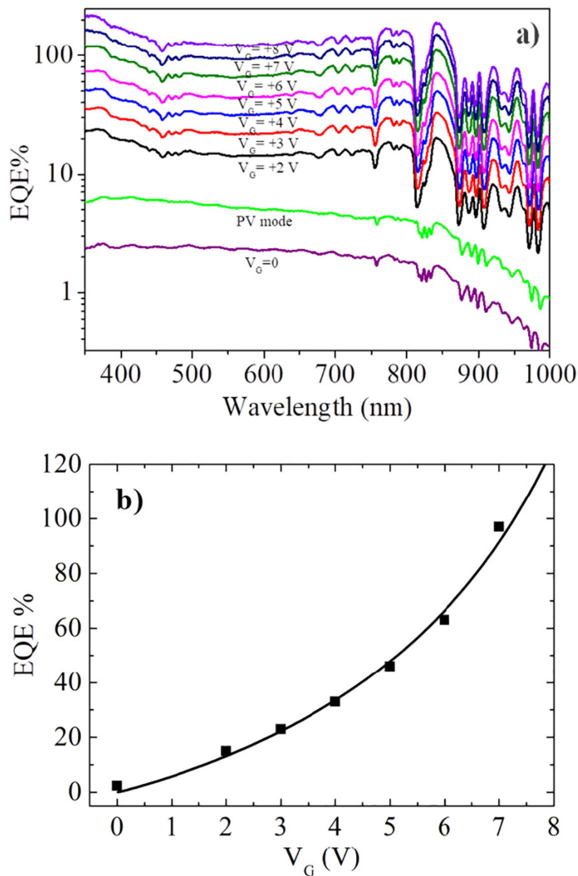

Fig. 6. a) External Quantum Efficiency (EQE) measured between S and D terminals as a function of the wavelength for using different values of V_G with $V_{SD} = 0$. Also shown for comparison is the EQE acquired in PV mode (green line); b) EQE vs. V_G as extracted by the data in a) at $\lambda = 500$ nm. The line is a fit to the data following the expression in Ref. [32] valid for avalanche photodetectors. (A colour version of this figure can be viewed online.)

measure a current flowing in the graphene which comes mainly from the photo-charges generated in the n-Si region of the device. This is confirmed by the EQE acquired in PV mode and reported in the same figure for comparison. The higher value obtained in the PV mode in the whole investigated λ range indicates that more photocharges are collected if compared to the PC mode for $V_G = 0$. However, by applying a gate voltage, an enhancement of the PD efficiency is obtained with the EQE increasing up to 200% for $V_G = +8$ V. The huge increase of EQE is clearly evidenced in Fig. 6b where the EQE measured at $\lambda = 500$ nm is shown as a function of V_G. The line is a fit to the data using the expression reported in Ref. [32] valid for avalanche PDs. The good agreement with the experimental data, although qualitative, confirms the presence of an avalanche mechanism [32], activated by the photogenerated charges, and indicates that this effect is predominant on the leakage contribution, which would show only a linear EQE vs. V_G dependence. Moreover, the observed huge increase of EQE when V_G is applied indicates that few holes recombine with electrons before to be collected by the electrodes.

The PDs have been tested using the pulsed laser source also in PC mode, acquiring measurements at different incident wavelengths, from $\lambda = 275$ nm up to $\lambda = 1150$ nm. A good linearity of the devices, below a saturation value, is confirmed by the peak current vs. light pulse energy reported in Fig. 7a. For a given energy, the photocurrent depends on the wavelength indicating that the number of the generated photocharges depends on λ. This

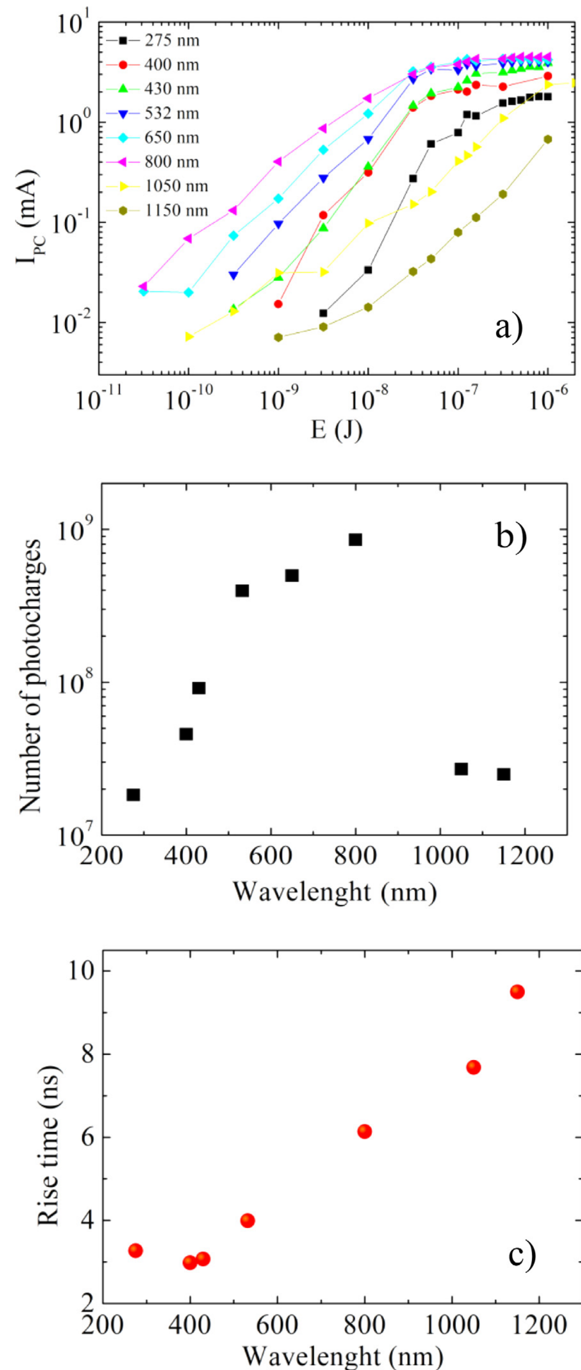

Fig. 7. a): photocurrent peak value vs. fs laser light pulse energy measured at different wavelengths in PC mode with $V_G = 0$ and $V_{SD} = 0$; b): number of photocharges measured by the area under the peak current acquired in PC mode vs. wavelength at E = 10 nJ; c): rise time vs. wavelength in PC mode with $V_G = 0$ under 35 fs pulsed laser source for incident light energy $E = 10$ nJ. (A colour version of this figure can be viewed online.)

dependence is shown in Fig. 7b where the area under the acquired peak current is reported as a function of λ for $E = 10$ nJ. A similar behaviour is observed for all the investigated wavelengths in the linear regime as well as in the PV configuration. The number of generated photocharges increases up to $\lambda = 800$ nm and then decreases following the absorption spectrum of Si which lacks in absorbing infrared light.

In Fig. 7c the rise time vs. λ at $V_G = 0$ and $E = 10$ nJ is shown. As in

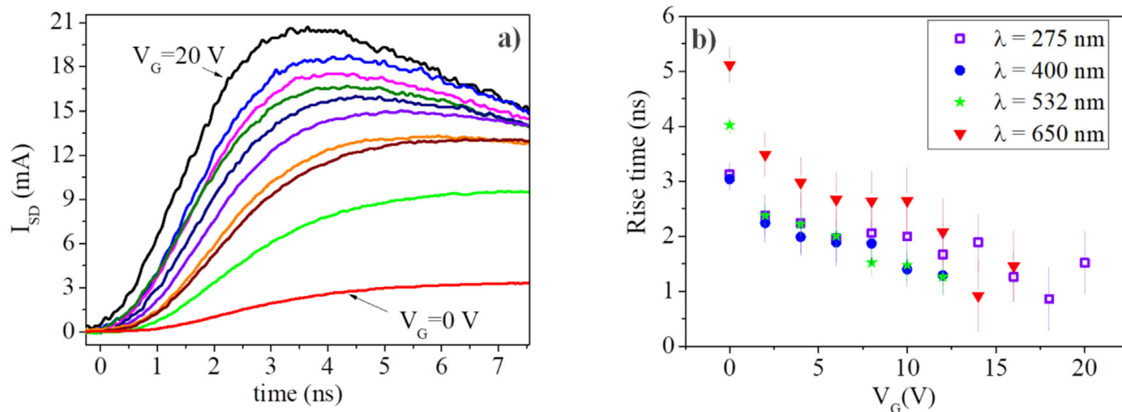

Fig. 8. a) Rise fronts of the curves I_{SD} vs. time in PC mode under $\lambda = 532$ nm illumination of the 35-fs pulsed laser, for V_G=0, 2 V, 6 V, 8 V, 10 V, 12 V, 14 V, 16 V, 18 V and 20 V from the bottom b) Rise time measured in PC mode between 10% and 90% of the rise fronts of the I_{SD} response to the pulsed laser as a function of V_G for different incident wavelengths. (A colour version of this figure can be viewed online.)

the case of the PV mode, the response time is constant at low λ and increases for $\lambda \geq 450$ nm suggesting a similar mechanism in the two different configurations at least for $V_G = 0$. Nevertheless, the PDs operating in the PC mode appear faster in their response to the light pulse with respect to the PV configuration. Even more interesting is the response of the detector to the pulsed laser when V_G is applied. Fig. 8a shows the response of the PD in PC mode at different V_G values when the incident laser pulse with $E = 10$ nJ and $\lambda = 532$ nm illuminates its active area. The curves are reported after subtracting the background due to the d.c. current component induced by V_G. Therefore, the data in Fig. 8a are representative of the response of the device to the fs light pulse, which is independent on any d.c. contribution. The current I_{SD} flowing through the graphene increases when the junction is in the avalanche regime with respect to the current measured at $V_G = 0$. Moreover, increasing V_G a decrease in the time response is clearly observed by the decrease of the rise time of the same curves. This is measured (by considering the time difference between 90% and 10% of the whole signal) and reported in Fig. 8b for all the investigated wavelengths. Rise time values of the order of 1 ns are reached for the highest applied V_G.

4. Discussion

The response time is related to the time required to the photocharges, generated at a depth L inside the photodetector, to be collected by the electrodes [33]. Due to the high transparency of graphene in all the investigated λ range, one can assume that most of the light is absorbed inside the Si substrate and that graphene acts as a conductive transparent window. Since L depends on the light wavelength λ through the Si optical absorption coefficient [34], then it is expected that τ_r depends on λ as shown in the inset of Fig. 4 and in Fig. 7c for the PV and PC configurations respectively. In the case of our experiment, the penetration depth L for the graphene/Si interface ranges between $L = 10^{-2}$ µm and $L = 10^3$ µm for $\lambda = 250$ nm and $\lambda = 1100$ nm respectively.

When in contact with doped Si, graphene gives rise to a rectified interface. Fig. 9a gives a qualitative sketch of the energy levels at the graphene/Si interface. After light absorption in the n-Si substrate, the photocharges are separated by the built-in potential V_{bi} which drives the holes towards the graphene layer and the electrons towards the G electrode. The action of V_{bi} is confined inside the depletion zone which starts from the interface and extends inside the Si for a depth W. Depending on the distance L from the surface where the photocharges are generated, two different main mechanisms have to be considered in Si as responsible for the motion of the holes towards the surface: drift and diffusion [35]. The holes generated at a distance $L \leq W$ are drifted towards the surface by the action of V_{bi}. The holes generated beyond the depletion layer at a depth $L \geq W$ are carried by a diffusion mechanism up to the edge with the depletion layer and, when at the

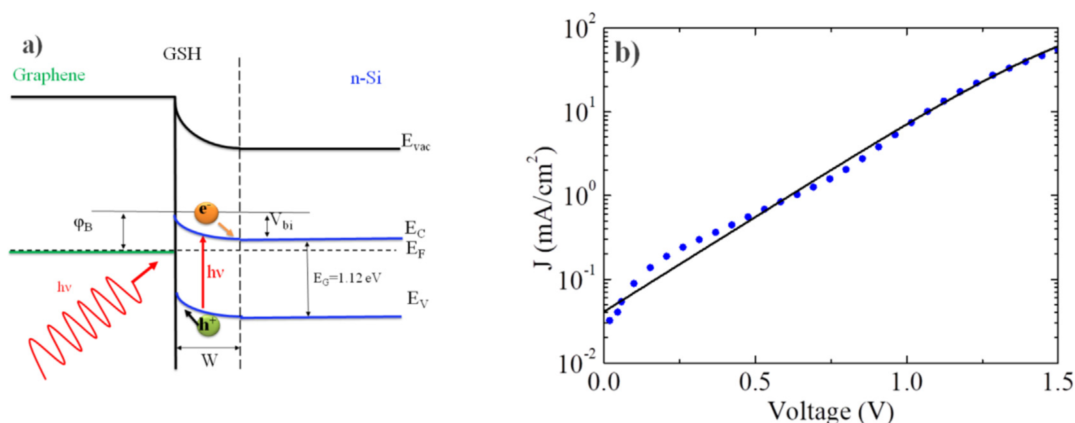

Fig. 9. a) Schematic of the band diagram of the GSH showing the barrier potential ϕ_B, the built in potential V_{bi} and the depletion layer W. b) Same data of Fig. 3 in semilogarithmic scale for $V > 0$. The line is a fit to the data by using equation (1). (A colour version of this figure can be viewed online.)

distance W from the surface, they are drifted towards the graphene layer. In both the cases, once the holes have reached the graphene counter electrode, they diffuse along this layer to reach the metallic interdigitated electrodes. Therefore, the maximum path the holes have to travel to be collected by the interdigitated electrodes is $L+d/2$ where $d=200\,\mu m$ is the distance between two adjacent electrode edges. In order to make our speculation more quantitative, a deeply analysis of our GSH is needed.

From the STM/STS analysis (see Fig. 2b), we argue that the graphene layer transferred on the Si surface has a metallic nature. Therefore, the GSH can be treated as a Schottky junction in agreement with most of the literature data on the same argument [8,34–38]. Following the general theory of the Schottky junctions [32], the *I-V* characteristics are well approximated by the expression:

$$J = J_0\ \exp\left[\frac{q(V-JAR_S)}{nk_BT}\right] \tag{1}$$

Where J is the current density, $J_0 = A^*T^2e^{-q\varphi_B/k_BT}$ is the saturation current density, n the ideality factor, k_B is the Boltzmann constant, T the temperature, q the elementary charge, A is the junction area and R_S its electrical resistance. The fit to the data of the *I-V* characteristic acquired in dark conditions and shown in Fig. 3a for $V>0$ using expression (1), with n, J_0 and R_S as fitting parameters, is reported in Fig. 9b. The fitting procedure gives $n=7.3$, $R_S=1.8\,k\Omega$ and $J_0=41\,\mu A$. A such high value of n is usually ascribed to charge image effects into graphene and it is in agreement with that obtained by other authors in Schottky GSH [8,37], while R_S is of the same order of that measured for our devices. Assuming a Richardson constant $A^*=110\,A\,cm^{-2}\,K^{-2}$ valid for Si, the value $\phi_B=0.48\,V$ is obtained for the barrier potential by the expression of J_0. Although this value is purely indicative due to several parameters assumed for its evaluation, it is consistent with the work function of graphene which is given by $\varphi_{gr}=\varphi_B+\chi_{Si}$ where $\chi_{Si}=4.05$ eV is the electron affinity of Si [32]. The calculation gives $\phi_{gr}=4.5$ eV in very good agreement with the values reported for graphene [37]. The width of the depletion zone in a Schottky junction is given by:

$$W = \sqrt{\frac{2\varepsilon_{Si}\varepsilon_0 V_{bi}}{qN_D}} \tag{2}$$

where $\varepsilon_{Si}=11.7$ and $\varepsilon_0=8.85\times10^{-14}\,F/cm^2$ are the permittivity in Si and in vacuum respectively. Considering for V_{bi} the expression $V_{bi}=\varphi_B-(k_BT/q)\ln(N_C/N_D)$ where $N_C=2.8\times10^{19}cm^{-3}$ is the density of the states at conduction band for Si, one obtains $V_{bi}=0.28\,V$ and, as a consequence, $W=0.2\,\mu m$. It is worth noting that this value satisfies the condition $L\approx W$ for $\lambda=450$ nm which is with a very good approximation the value at which a change in the slope of τ_r vs. λ reported in the inset of Fig. 4 and in Fig. 7c is observed. This result suggests that for $\lambda\le450$ nm the photocharges are generated inside the depletion zone ($L\le W$) while for $\lambda\ge450$ nm results $L\ge W$ and the photocharges generated beyond the depletion zone add their contribution to the photocurrent.

The time required for the charges to cross the depletion zone under the action of the potential V_{bi} is $t_{dr}=W/v_{dr}$ where $v_{dr}=\mu V_{bi}/W$ is the drift velocity. Considering the calculated values for V_{bi} and W and taking $\mu=400\,cm^2/V\cdot s$ as the mobility of the holes in n-Si [32] with the given donor concentration, one obtains $t_{dr}\approx10^{-12}$ s which is too low to be associated to the response time measured in our PDs. This calculation suggests that the drift mechanism can be considered negligible and that the holes generated at the depth $L\le W$ spend most of their time to reach the interdigitated electrodes along the graphene layer.

It can be useful to analyse the τ_r vs. λ dependence shown in Fig. 7c for the PC configuration because in this case only the top interdigitated electrodes collect the photocharges and we can neglect the electrons that diffuse towards the G bottom electrode. In this case, for $\lambda\le450$ nm, which means for charges generated inside the depletion zone ($L\le W$), $\tau_r=3$ ns is measured. Assuming for the graphene mobility the value $\mu = 1\times10^5\,cm^2/V\cdot s$ [4], a diffusion length $L_p=\sqrt{(k_BT/q)\mu\tau_r}\cong30\mu m$ entirely along the graphene counter electrode is obtained. The charges emerging in the graphene layer at a longer distance from the electrode scarcely participate to the photocurrent being lost probably for recombination mechanism enhanced by the n-doping of graphene and by the boundary between different graphene sheets present in the surface layer as evidenced by STM. Increasing λ the light penetration depth L increases but for $L\le W$ the main mechanism is the diffusion in the graphene layer being the drift time negligible. Since the diffusion time in graphene does not depend on λ, a constant behaviour of τ_r vs. λ is expected for $\lambda\le450$ nm ($L\le W$) as confirmed by the data reported in Fig. 7c. For a further increase of λ, the photocharges are generated outside the depletion zone ($L\ge W$) up to the maximum possible distance from the interface corresponding to the whole substrate thickness ($L=10^3\,\mu m$ for the highest measured $\lambda=1150$ nm). At this wavelength, the data in Fig. 7c indicate that only the holes generated within a depth $L_p\approx3\,\mu m$, corresponding to $\tau_r=10$ ns, reach the surface and are collected by the electrodes.

When $V_G>0$ V, the photogenerated holes reach the graphene counter electrode in a shorter time compared to the condition $V_G=0$ because a charge drift velocity, which increases with V_G, adds to the diffusive velocity, thus making the detector faster as V_G increases. The data in Fig. 8b confirm this trend for all the wavelengths. Moreover, there is a reduction of the difference in the response speed for different λ when the device is in the avalanche region ($V_G>4$ V). For $V_G=0$ the rise time for $\lambda=275$ nm is about 3 ns and for $\lambda=650$ nm it is 5 ns but increasing V_G for both values of λ the rise times decrease down to about 1 ns for $V_G=15$ V. Indeed, when the device is in this operating condition, there are two effects to consider already described above: the increase in the velocity given by the effect of the electric field in the avalanche regime and the longer response times for longer λ due to the increase in the path length caused by an increase of L at longer wavelength. When V_G exceeds about 4 V, the former effect (speed increase) prevails on the latter (path length increase) and the response starts to become the same for all the incident λ.

In the case of the PV configuration, the electrodes used for the charge collections are the top shorted S-D and the bottom G. In all the cases ($L\le W$ or $L\ge W$) the electrons, separated by V_{bi}, have to cross the whole Si substrate to give rise to the signal detection and this entails an increasing of the response time. For $\tau_r=18$ ns, corresponding to $\lambda\le450$ nm, the holes travel for a distance $L_p=43\,\mu m$ and the electrons (having a higher mobility $\mu=10^3\,cm^2/V\cdot s$ [32]) travel for $L_e=68\,\mu m$, both distances comparable with the Si substrate thickness. During this time, the holes are collected by the top S-D electrodes and the electrons by the bottom G electrode. Increasing λ, L increases and, as in the PC configuration, the time required for collecting the photogenerated charges increases giving rise to the τ_r vs. λ behaviour shown in the inset of Fig. 4. Nevertheless, even though the PD contacted in PV mode is slower than the PC configuration, it presents a higher efficiency, as shown in Fig. 6, due to the higher number of collected photocharges at least if compared to the PC PDs working at $V_G=0$.

In the above discussion the possible dependence of τ_r on the number of the generated photocharges has not been taken into account. This is consistent with the data shown in Fig. 7b where the number of photocharges collected by the electrodes is reported as a

Table 1
Key parameters of our samples compared with a commercial photodetector and two recent graphene based devices.

Photodetector	Active Area(mm^2)	Responsivity A/W	Breakdown voltage (V)	Capacitance nF	Rise Time ns	Spectral range (nm)	Ref.
Hamamatsu SiAPD S12053	0.8	0.50	200	5 × 10-3	1.5	300–1000	31
Graphene/Si	10^{-3}	10^5			3×10^4		38
Graphene/Si	0.25	0.14		1.6 × 10-2	4	300–1100	21
Our device	8	0.66–0.75 (±0.01)	~4	5.1 ± 0.1	1–10 (±0.1)	270–1150	This work

function of the wavelength. Following this behaviour, a dependence of τ_r on the number of photocharges should show a change in τ_r vs. λ at $\lambda \geq 800$ nm which is not observed experimentally. This supports our interpretation that τ_r mainly depends on the path length covered by the photocharges instead of their density.

Our interpretation of the experimental results suggests that the use of the three electrode configuration plays a decisive role on the PD performance reducing the response time and increasing the photocurrent in the avalanche regime. Here the doped Si represents the absorbing layer while graphene plays the triple role of light transmitter, junction counter electrode (participating to the formation of the built-in potential V_{bi} at the interface) and photocarrier collector.

A list of some key parameters of our samples is reported in Table 1 in comparison to that present on datasheets of a commercial PD and to the state of the art of some graphene/Si based devices. With respect to commercial Si based PDs our device presents a much lower breakdown voltage, a higher responsivity and almost the same time response. Also interesting is the comparison with some recent studied graphene/Si PDs one with high responsivity and the other with a low rise time. Our devices are the only ones that show at the same time a good response time and a quite satisfactory responsivity. The high value of the junction capacitance reported for our devices is due to the large active area. Among the different methods that can be adopted to improve the PD performance, a reduction of the active area for reducing the capacitance as well as the interface inhomogeneity can be explored. This certainly would give a shorter rise time (capacitive effects) and a uniform barrier potential (homogeneity of the interface) with a consequent reduction of the leakage current. A different geometry of the interdigitated electrodes could be a better approach with respect to the possibility to increase the number of fingers since this method has already been explored [25] and in that view the adopted device represents an optimization between the possibility to have the maximum of collected charges avoiding detrimental effects due to the consequent covering of the active area. A further improvement of the PD performance can be obtained by enhancing the graphene quality by reducing the number of layers and, as a consequence, the scattering rate of the photocharges in their path towards the electrodes. Finally, since the absorption process mainly happens inside the Si substrate, PDs sensitive to a different λ range can be obtained by substituting Si with other semiconductors for response shifted in a different wavelength range. From this point of view, since the PD is based on a rectified junction obtained by depositing graphene on doped Si surface, any other material can be used [37] with the perspective to increase the photocurrent, reduce the response time or change the absorption wavelength range.

5. Conclusions

In conclusion, we reported on a photodetector based on GSH provided with three electrodes for both photovoltaic and photoconductive measurements. In dark conditions, the device shows rectifier properties due to the formation of a metal/semiconductor Schottky barrier. In both configurations used, the device is able to detect fast signals in a range of wavelengths ranging from near UV to near IR which makes it very promising for many fast detection applications. A difference in the PD's rise time has been shown between the PV and the PC mode, due to a different path of the photogenerated charges at the junction. In PC mode, it has been shown that thanks to the gate electrode it is possible to make holes doping within the graphene that increases the EQE values up to 200% and decreases the rise time to about 1 ns. These values result higher than other graphene and carbon nanostructures based three terminal devices. The obtained results support our design of the interdigitated electrodes that reduce the path length of the charges collected by graphene while the three contacts configuration allows to amplify the signal after light absorption.

Acknowledgments

M. Scagliotti, M. Salvato and M. De Crescenzi would like to acknowledge the European Community for the HORIZON2020 MSC-RISE Project DiSetCom (GA823728). I.V. Komissarov and S.L. Prischepa acknowledge financial support of the “Improving of the Competitiveness” Program of the National Research Nuclear University MEPhI (Moscow Engineering Physics Institute).

References

[1] A.H. Castro Neto, F. Guinea, N.M.R. Peres, K.S. Novoselov, A.K. Geim, The electronic properties of graphene, Rev. Mod. Phys. 81 (2009) 109–162.
[2] F. Bonaccorso, Z. Sun, T. Hasan, A.C. Ferrari, Graphene photonics and optoelectronics, Nat. Photon. 4 (2010) 611–622.
[3] A.K. Geim, K.S. Novoselov, The rise of graphene, Nat. Mater. 6 (2007) 183–191.
[4] L. Wang, I. Meric, P.Y. Huang, Q. Gao, Y. Gao, H. Tran, et al., One dimensional electrical contact to a two-dimensional material, Science 342 (2013) 614–617.
[5] V. Ryzhii, M. Ryzhii, D. Svintsov, V. Leiman, V. Mitin, M.S. Shur, T. Otsuji, Infrared photodetectors based on graphene van der Waals heterostructures, Infrared Phys. Technol. 84 (2017) 72–81.
[6] A. Di Bartolomeo, G. Luongo, L. Iemmo, F. Urban, F. Giubileo, Graphene-silicon Schottky diodes for photodetection, IEEE Trans. Nanotechnol. 17 (2018) 1133–1137, https://doi.org/10.1109/TNANO.2018.2853798.
[7] S. Riazimehr, S. Kataria, R. Bornemann, P.H. Bolivar, F.J.G. Ruiz, O. Engstrom, A. Godoy, M.C. Lemme, High photocurrent in gated graphene-silicon hybrid photodiodes, ACS Photonics 4 (6) (2017) 1506–1514, https://doi.org/10.1021/acsphotonics.7b00285.
[8] Chun-Chung Chen, Mehmet Aykol, Chia-Chi Chang, A.F.J. Levi, B. Cronin Stephen, Graphene-silicon Schottky diodes, Nano Lett. 11 (2011) 1863.
[9] L.P. Yu, M. Batmunkh, T. Grace, M. Dadkhah, C. Shearer, J. Shapter, Application of a hole transporting organic interlayer in graphene oxide/single walled carbon nanotube–silicon heterojunction solar cells, J. Mater. Chem. 5 (2017) 8624–8634.
[10] F. Liu, S. Kar, Quantum carrier reinvestment-induced unltrahigh and broadband photocurrent responses in graphene-silicon junctions, ACS Nano 8 (2014) 10270–10279.
[11] B.B. Lahiri, S. Bagavathiappan, T. Jayakumar, J. Philip, Medical applications of infrared thermography: a review, Infrared Phys. Technol. 55 (2012) 221–235.
[12] T. Mueller, F. Xia, P. Avouris, Graphene photodetectors for high-speed optical communications, Nat. Photon. 4 (2010) 297–301.
[13] V. Ryzhii, T. Otsuji, V.E. Karasik, M. Ryzhii, V.G. Leiman, V. Mitin, M.S. Shur, Comparison of intersubband quantum-well and interband graphene-layer infrared photodetectors, IEEE J. Quantum Electron. 54 (2018) 4000108.
[14] H. Chen, K. Liu, L. Hu, A.A. Al-Ghamdi, X. Fang, New concept ultraviolet photodetectors, Mater. Today 18 (2015) 493–502.
[15] K.F. Mak, M.Y. Sfeir, Y. Wu, C.H. Lui, J.A. Misewich, T.F. Heinz, Measurements of the optical conductivity of graphene, Phys. Rev. Lett. 101 (2008), 196405 1-4.

[16] P. Spinelli, V.E. Ferry, J. van de Groep, M. van Lare, M.A. Verschuuren, R.E.I. Schropp, et al., Plasmonic light trapping in thin-film Si solar cells, J. Opt. 14 (2012), 024002 1-02400211.
[17] X. Gan, K.F. Mak, Y. Gao, Y. You, F. Hatami, J. Hone, et al., Strong enhancement of light-matter interaction in graphene coupled to a photonic crystal nanocavity, Nano Lett. 12 (2012) 5626–5631.
[18] M. Furchi, A. Urich, A. Pospischil, G. Lilley, K. Unterrainer, H. Detz, et al., Microcavity-integrated graphene photodetector, Nano Lett. 12 (2012) 2773–2777.
[19] X. Gan, R.J. ye Shiue, Y. Gao, I. Meric, T.F. Heinz, K. Shepard, et al., Chip-integrated ultrafast graphene photodetector with high responsivity, Nat. Photon. 7 (2013) 883–887.
[20] Z. Sun, Z. Liu, J. Li, G. Tai, S.P. Lau, F. Yan, Infrared photodetectors based on CVD-grown graphene and PbS quantum dots with ultrahigh responsivity, Adv. Mater. 24 (2012) 5878–5883.
[21] Xia Wan, Yang Xu, H. Guo, K. Shehzat, A. Alio, Y. Liu, et al., A self-powered high-performance graphene/silicon ultraviolet photodetector with ultra-shallow junction: breaking the limit of silicon, 2D Mater. Appl. 1 (2017) 4, https://doi.org/10.1038/s41699-017-0008-4.
[22] A. Bagolini, M. Boscardin, P. Conci, M. Crivellari, G. Giacomini, F. Mattedi, et al., Micromachined silicon radiation sensors-part 2: fabrication technologies, in: XVIII AISEM Annual Conference, 2015, pp. 1–4.
[23] F. De Nicola, M. Salvato, C. Cirillo, M. Crivellari, M. Boscardin, M. Passacantando, et al., 100% internal quantum efficiency in polychiral single-walled carbon nano tube bulk heterojunction/silicon solar cells, Carbon 114 (2017) 402–410.
[24] M. Salvato, M. Scagliotti, M. De Crescenzi, M. Crivellari, P. Prosposito, I. Cacciotti, P. Castrucci, Single walled carbon nanotube/Si heterojunctions for high responsivity photodetectors, Nanotechnology 28 (2017), 435201 1-9.
[25] M. Scagliotti, M. Salvato, M. De Crescenzi, M. Boscardin, P. Castrucci, Influence of the contact geometry on single-walled carbon nano tube/Si photodetector response, Appl. Nanosci. 8 (2018) 1053–1058.
[26] I.V. Komissarov, N.G. Kovalchuk, V.A. Labunov, K.V. Girel, O.V. Korolik, M.S. Tivanov, et al., Nitrogen-doped twisted graphene grown on copper by atmospheric pressure CVD from decane precursor, Beilstein J. Nanotechnol. 8 (2017) 145–158.
[27] I.V. Komissarov, N.G. Kovalchuk, E.A. Kolesov, M.S. Tivanov, O.V. Korolik, A.V. Mazanik, et al., Micro Raman investigation of graphene synthesized by atmospheric pressure CVD copper foil from decane, Phys. Procedia 72 (2015) 450–454.
[28] G. Cerullo, S. De Silvestri, Ultrafast optical parametric amplifiers, Rev. Sci. Instrum. 74 (2003) 1.
[29] L. Tian, L. di Mario, V. Zannier, D. Catone, S. Colonna, P. O'Keeffe, et al., Ultrafast carrier dynamics, band-gap renormalization, and optical properties of ZnSe nanowires, Phys. Rev. B 94 (2016) 1–8, 165442.
[30] F. Toschi, D. Catone, P. O'Keeffe, A. Paladini, S. Turchini, J. Dagar, T.M. Brown, Adv. Funct. Mater. 28 (2018) 1707126.
[31] See Hamamatsu Handbook at. https://www.hamamatsu.com/sp/ssd/doc_en.html.
[32] S.M. Sze, Physics of Semiconducting Devices, vol 282, Wiley, New York, NY, USA, 1969.
[33] A.O. Goushcha, B. Tabbert, On response time of semiconductor photodiodes, Opt. Eng. 56 (2017), 097101.
[34] C.C. Chen, M. Aykol, C.C. Chang, A.F.J. Levi, S.B. Cronin, Graphene-silicon Schottky diodes, Nano Lett. 11 (2011) 1863–1867.
[35] S. Kobayashi, Y. Anno, K. Takei, T. Arie, S. Akita, Photoresponse of graphene field-effect-transistor with n-type Si depletion layer, Sci. Rep. 8 (2018) 4811, https://doi.org/10.1038/s41598-018-22974-7.
[36] A. Di Bartolomeo, Graphene Schottky diodes: an experimental review of the rectifying graphene/semiconductor heterojunction, Phys. Rep. 606 (2016) 1–58.
[37] S. Tongay, M. Lamaitre, X. Miao, B. Gila, B.R. Appleton, A.F. Hebard, Rectification at graphene-semiconductor interfaces: zero-gap semiconductor-based diodes, Phys. Rev. X 2 (2012), 011002, 1-10.
[38] J. Liu, Y. Yin, L. Yu, Y. Shi, D. Liang, D. Dai, Silicon-graphene conductive photodetector with ultra-high responsivity, Sci. Rep. 7 (2017), https://doi.org/10.1038/srep40904.